# Interplay of hydrogen boride sheets with water: An insight into edge stability

Kurt Irvin M. Rojas [1,*] Yoshitada Morikawa [1,2] and Ikutaro Hamada [1,†]

[1]*Department of Precision Engineering, Graduate School of Engineering, Osaka University, 2-1 Yamadaoka, Suita, Osaka 565-0871, Japan*

[2]*Research Center for Precision Engineering, Graduate School of Engineering, Osaka University, 2-1 Yamadaoka, Suita, Osaka 565-0871, Japan*

(Received 29 July 2024; accepted 1 November 2024; published 27 November 2024)

Hydrogen boride (HB) sheets, a two-dimensional material composed of hexagonal boron (B) with bridging hydrogen (H), have recently been synthesized and shown significant potential in electronic devices and catalytic applications. Recent studies have shown that HB sheets are generally stable against water, in contrast to many boron hydride materials which undergo hydrolysis. This stability is attributed to the interplay between the negatively charged B and the strong B-B bond network. Despite this stability, experiments have shown that hydrolysis still takes place, albeit minimally. It is possible that the source of this minimal hydrolysis is related to regions with a less prominent B-B bond network; however, the microscopic details remain unclear. In this work, we investigated the various configurations of HB nanoribbon edges as representative of regions with less prominent B-B bond network and show their distinct region-specific behavior with water. We found that zigzag and armchair nanoribbons were generally stable against water, whereas in the case of the hydrogen-vacant armchair nanoribbon, an oxygen-boron bonding was observed, showcasing a chemisorption mechanism. Additionally, it was found that water dissociation is easier to proceed near the edge as opposed to the surface, signifying the more reactive nature of the edge. These results shed light on the mechanism of the partial hydrolysis observed in the experiment.

DOI: 10.1103/PhysRevMaterials.8.114004

## I. INTRODUCTION

A hydrogen boride (HB) sheet is a freestanding borophane material characterized by a six-membered boron ring and hydrogen atoms located on the bridge positions, maintaining a 1:1 stoichiometric ratio of hydrogen to boron. It can be synthesized from magnesium diboride ($MgB_2$) via $Mg^+/H^+$ ion exchange and liquid exfoliation [1,2]. The electron deficiency of the six-membered boron ring is resolved by the hybridization of two boron *p* orbitals and one hydrogen *s* orbital to form the three-center two-electron (3c-2e) bond, similar to boron hydrides [3]. However, in contrast to born hydrides, the HB sheet exhibits a negative boron charge state instead of a positive boron charge state, justifying its nomenclature [4,5].

The HB sheet exhibits intriguing physical and electronic characteristics that are applicable to a wide range of potential applications [6–11]. Unlike conventional boron hydrides, they possess chemical stability against water [5]. Furthermore, their notably high hydrogen content (8.5 wt.%) and ability to release these under ultraviolet irradiation [12–14] or through electrochemical means [15] makes them suitable for hydrogen storage applications [16–19]. In addition, they demonstrate exceptional catalytic performance [20–23], as evidenced by several studies showcasing their efficacy in facilitating the low-temperature conversion of ethanol (ethanol–ethylene) [24,25] and $CO_2$ ($CO_2$–methane/ethane) [26]. Moreover, they possess the capability to reduce specific metal ions, thereby facilitating the creation of nanocomposites [27,28]. Research into the diverse properties of HB sheets has paved the way for the development of new HB-based materials [4,29–37] and a range of applications, including batteries [38–41], sensors [42], and current limiters [43].

Initially, there were some concerns over its reactivity with water due to the issues associated with $MgB_2$'s interaction with water during the fabrication process [44]. In our previous study, HB sheet was found to be generally stable against water [5]. The stability can be attributed to the nonreactive negative charge state of boron which is protected by the covalent B-B bond network. Interestingly, on the first cycle of the water exposure experiment, small amounts of $H_2$ gas were recovered, signifying that some parts of the HB sheet sample have undergone hydrolysis. However, on the second cycle (after drying the sample at 393 K), the exposure no longer yielded $H_2$ gas, suggesting that hydrolysis did not occur and the reactive components of the samples were likely passivated. This passivation mechanism was further developed by Ito *et al.* [45] into a treatment method to produce pure HB sheet samples with long-term stability. The primary determinant of stability is the robust B-B bond network. Consequently, regions with less prominent B-B bond networks, such as large vacancy defects or edges, are expected to exhibit higher reactivity. While there is a possibility of hydrolysis occurring in these regions, microscopic details remain unclear.

This study centers on examining the interaction between water and HB sheets, particularly in regions with less prominent B-B bond networks, such as the edges. We utilized

*Contact author: krojas@cp.prec.eng.osaka-u.ac.jp
†Contact author: ihamada@prec.eng.osaka-u.ac.jp

 

density functional theory (DFT) calculations to investigate the edge regions by employing periodic HB nanoribbon (HBNR) models. Notably, we found that the orientation and termination of the edges are key factors in the formation of stable HBNRs. As for the interaction with water, unlike those observed on the surface, we identified distinct region-specific behaviors—both reactive and nonreactive. The small amount of hydrolysis observed in prior experiments could potentially be ascribed to the strong interaction seen in this work [5].

## II. METHODOLOGY

### A. Computational details

All calculations were conducted using DFT as implemented in the QUANTUM ESPRESSO software package [46–50]. The pseudopotentials generated using the Perdew-Burke-Ernzerhof formulation of the generalized gradient approximation were adopted from the GBRV ultrasoft pseudopotential library [51,52]. The exchange correlation functional was approximated using rev-vdW-DF2 to effectively account for the van der Waals interactions [53–55]. Kinetic energy cutoffs of 60 Ry and 480 Ry were used for the wave functions and augmentation charge, respectively. The HBNR edge directions and periodicity is oriented length-wise along the $x$ axis. The $k$ points were generated using the Γ-centered Monkhorst-Pack scheme with meshes of $11 \times 1 \times 1$ and $27 \times 1 \times 1$ for structural optimization and electronic structure calculations of a HBNR unit length, respectively. When expanding the nanoribbon into a supercell along its periodic direction, the $k$-point meshes were adjusted accordingly to ensure a consistent $k$-point density. The vacuum spacing of ca. 16 Å was added along the non-periodic directions. The force and energy criteria for convergence in structural optimizations were set to $10^{-4}$ Ry·Bohr$^{-1}$ and $10^{-5}$ Ry, respectively. Lastly, small random atomic displacements were introduced to prevent the formation of symmetry-induced metastable configurations.

### B. Nanoribbon structural model

All HBNR structures were generated from the optimized HB sheet structure using rev-vdW-DF2, as provided in Ref. [5]. In this study, we employed HBNRs with armchair (ACNR) and zigzag (ZZNR) edges from the rectangular unit cell as illustrated in Fig. 1. To investigate the stability of HBNR with different edges and terminations, we built a $(4 \times 5)$ HB supercell along $x$ and $y$ directions, respectively. For simplicity, the edge directions and the periodicity were realigned along the $x$ axis. A supercell size of four along the periodic direction effectively minimizes self-interactions for both water adsorption and hydrogen vacancies (Fig. S1 [56]), providing reliable energy values without excessive computational overhead. Lastly, we terminated it along the nonperiodic $y$ direction to create the ZZNR and ACNR models.

To investigate the interaction between water and HB edges with different terminations, we employed "asymmetric" HBNR models, resembling the asymmetric slab, to model a solid surface in which atoms in the bottom layers are constrained to their bulk positions, thereby a "constrained" nanoribbon model. The constructed constrained ACNR ($c$ACNR) comprises of four unit cells in the periodic

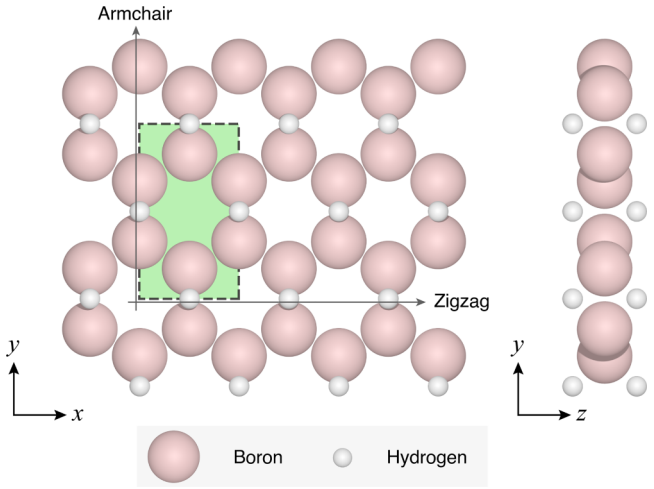


FIG. 1. Model of the HB sheet. The green region indicates the rectangular unit cell of the HB sheet. Edge directions for armchair and zigzag nanoribbons are also indicated.

($x$) direction and five atomic chains stacked along the non-periodic $y$ direction, while the constrained ZZNR ($c$ZZNR) comprised of four unit cells in the periodic ($x$) direction and ten atomic chains in the non-periodic ($y$) directions.

In the HBNR models, we investigate the optimal amount of hydrogen termination needed for each edge boron atom to stabilize and passivate the dangling bonds at the edge of the nanoribbons. The primary focus is identifying the most stable structures among various edge terminations, determined by their formation energy. This approach provides insights into the configurations that are most likely to appear in experimental conditions. The formation energy is defined as

$$E_f = \frac{1}{2L_{NR}}\left[E_{NR} - \frac{N_H}{2}\cdot\mu_{H_2} - \left(N_{HB}\cdot E_{HB} - \frac{N_H^{\dagger}}{2}\cdot\mu_{H_2}\right)\right], \tag{1}$$

where $L_{NR}$ and $\mu_{H_2}$ denote the length of the nanoribbon supercell in the periodic direction and the chemical potential of gas-phase $H_2$, respectively. $E_{NR}$ and $E_{HB}$ represent the total energy of the HBNR and that of the HB sheet with the rectangular unit cell (Fig. 1), respectively. $N_{HB}$, $N_H$, and $N_H^{\dagger}$ correspond to the number of unit cells required to construct the nanoribbon, the number of hydrogen terminating the edge and the number of hydrogen removed to form a non-H-terminated nanoribbon, respectively. The inclusion of the corrective term involving $N_H^{\dagger}$ is necessary for properly referencing and aligning the formation energies to the non-H-terminated structure. Further details on the derivation are provided in Eq. (S2) [56].

### C. Interaction quantities

The interaction between the nanoribbon and water was thoroughly examined, and two key quantities were calculated to characterize it. The first quantity is the adsorption energy defined as

$$E_{ads} = E_{NR} + E_{molecule} - E_{NR/molecule}, \tag{2}$$

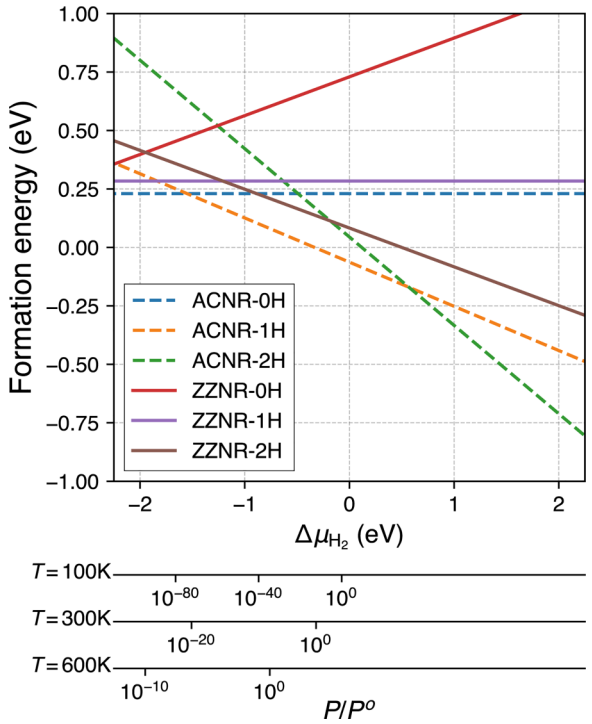


FIG. 2. Formation energies of various HB nanoribbons as functions of $H_2$ chemical potential. The main axis represents the chemical potential relative to the to the total energy of gas-phase $H_2$, denoted as $\Delta\mu_{H_2} = \mu_{H_2} - E_{H_2}$. The bottom axes show corresponding $H_2$ pressures ($P$'s) at different temperatures ($T$'s) normalized by $P^\circ$ ($P^\circ = 0.1$ MPa), which are obtained using the equation $\Delta\mu_{H_2} = H^\circ(T) - H^\circ(0) - TS^\circ + k_B T \ln(P/P^\circ)$ [57,58].

where $E_{NR}$, $E_{molecule}$, and $E_{NR/molecule}$ represent the total energies of the nanoribbon, molecule, and molecule adsorbed on the nanoribbon, respectively. In this definition, a positive $E_{ads}$ indicates that the adsorbate undergoes an exothermic adsorption process.

Second, the charge-related quantities, such as charge density and Löwdin charges, were utilized to analyze the resulting changes in electron distribution following adsorption. The charge density difference was investigated, which is defined as

$$\Delta\rho = \rho_{NR/molecule} - \rho_{molecule} - \rho_{NR}, \quad (3)$$

where $\rho_{NR/molecule}$ represents the charge density of the molecule-adsorbed nanoribbon, while $\rho_{molecule}$ and $\rho_{NR}$ refer to the charge densities of isolated molecule and nanoribbon in their adsorbed geometries, respectively.

## III. RESULTS AND DISCUSSION

### A. Edge terminations

The diversity in edge terminations is a significant concern, given the unknown stability of these structures; therefore, the need to investigate their relative stability. We considered the ratios of H/B = 0, 1, 2 at the edges referred to as 0H, 1H, and 2H, for the ZZNR and ACNR, representing varying levels of hydrogen saturation. Figure 2 illustrates the formation energy as a function of chemical potential of $H_2$, referenced to the total energy of gas-phase $H_2$ at 0 K ($\Delta\mu_{H_2}$). The secondary axes indicate the corresponding $H_2$ pressures at different temperatures.

Herein, various edge terminations are compared to identify those with the lowest formation energy, signifying their relative ease of formation. It was found that the ACNR − 1H exhibits the lowest formation energy, specifically at $\Delta\mu_{H_2} \sim 0$. However, as the chemical potential deviates toward lower and higher chemical potential regions, the preference shifts to ACNR − 0H and ACNR − 2H, respectively. For the zigzag edge, the ZZNR − 2H configuration emerges as the most favorable at $\Delta\mu_{H_2} \sim 0$. However, as the chemical potential decreases, preference transitions to ZZNR − 1H, followed by ZZNR − 0H at even lower chemical potentials. Among the two edge types, ACNR demonstrates a strong preference at all chemical potential ranges.

The reason for preference on the hydrogen-boron termination ratio is primarily related to the dangling bond. For ZZNR, boron atoms, initially stabilized by two 3c-2e bonds, require two electrons for bonding. Conversely, in the ACNR case, the boron atoms were previously stabilized by another covalently bonded boron, necessitating only one electron for stabilization. In light of these findings, the ACNR − 1H and ZZNR − 2H were selected to represent each class of edge orientations, as they exhibit a strong preference in the region near $\Delta\mu_{H_2} = 0$ and will be used for further investigations, particularly in exploring their interactions with water.

The optimized structures of ACNR − 1H and ZZNR − 2H are illustrated in Fig. 3(a). All optimized structures are presented in Fig. S2 [56]. The structure of the ACNR − 1H remained largely unchanged compared to the pristine HB sheet surface. On the contrary, ZZNR − 2H underwent a significant reconstruction, resulting in a fringelike structure along the edge hexagonal ring. This fringelike structure has not been observed in the previous literature on HBNRs [7,36], possibly due to the limitation in the model size or symmetry-induced metastability of an "ordered" edge configuration. From the charge perspective, there were no shifts in charge state along the fringelike edge despite the structural alterations, meaning the edge remains stable (see Fig. S3 [56]). Interestingly, the fringing was only localized to the outermost ring and did not proliferate throughout the nanoribbon body.

With the ACNR − 1H and ZZNR − 2H structures as a base, the constrained version of the structures were constructed to further evaluate the edge's interaction with water. The constrained ACNR ($c$ACNR) and constrained ZZNR ($c$ZZNR) is shown in Figs. 3(b) and 3(c). In addition, a single hydrogen vacancy was created to induce a possible reactive site. Upon optimization, the hydrogen vacant constrained ZZNR ($H_v$-$c$ZZNR) did not change much, however, the hydrogen vacant constrained ACNR ($H_v$-$c$ACNR) led to a collapse of the outer hexagon. This is primarily caused by inadequate passivation for the electron-deficient boron atom which is a recurrent issue in the formation of borophene polymorphs, where many synthesis methods often used an ion or metal substrate as an electron donor to stabilize the borophene sheet [59]. The structure was further examined using Löwdin charges. As shown in our previous study [5], the charge state of B atoms changes from negative to positive upon the

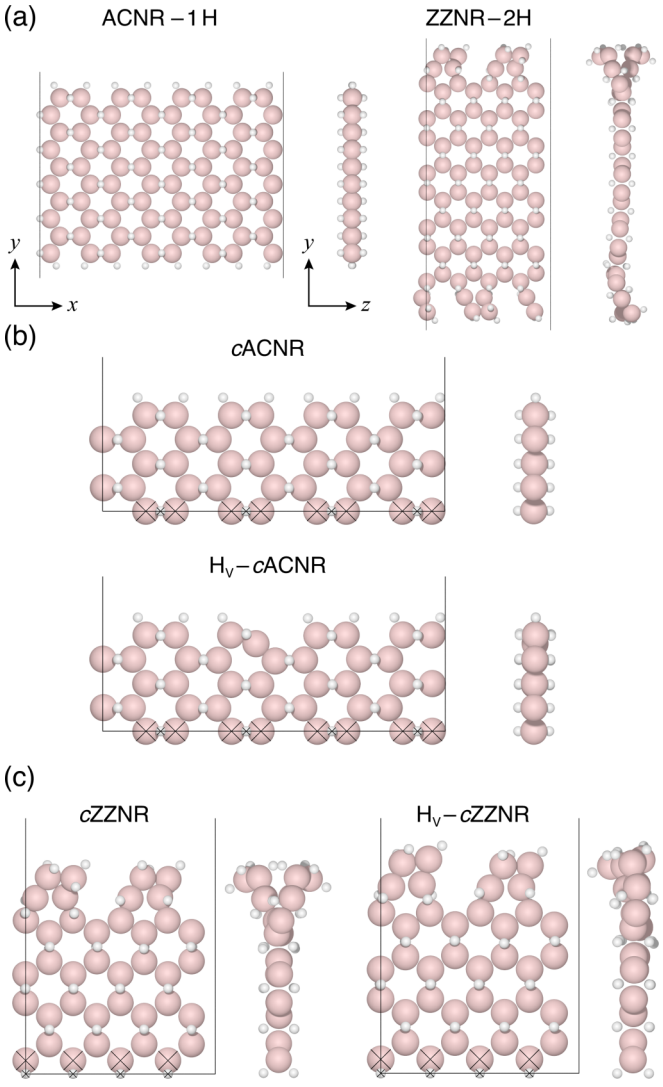


FIG. 3. Optimized structures of the HB nanoribbons. (a) Structures of the most stable configurations for ACNR − 1H and ZZNR − 2H. (b) Structures of *c*ACNRwithout and with hydrogen vacancy ($H_v$). (c) Structures of *c*ZZNR without and with $H_v$.

dissociation of $B_2H_6$ (diborane) to $BH_3$ (borane). This shift to a positive charge state precipitates the onset of hydrolysis by favorably attracting the oxygen atom of water. At the HB sheet surface, the charge states do not easily change, even with small vacancy defects, due to the B-B network present in the system. However, in the case of $H_v$-*c*ACNR, the Löwdin charge of one of the edge B atoms was found to be 2.917 e (less than three) as compared with that of a B atom at the HB sheet surface (3.140 e [5]), suggesting a positive charge state (see Fig. S4 and Table S1 [56]). The manifestation of positive charge state is likely associated with the less prominent B-B network near the edges.

### B. Water interaction with armchair and zigzag edges

A water molecule was introduced at various edge sites in different initial rotational configurations. The calculated adsorption energies for each adsorption systems are summarized in Table I. The adsorption energies for *c*ACNR, *c*ZZNR, and $H_v$-*c*ZZNR fall within the range of physisorption. In contrast, the adsorption energy for the $H_v$-*c*ACNR is 1.03 eV, which lies within the chemisorption energy range, suggesting the occurrence of chemical bonding.

TABLE I. Adsorption energies for water on various HB nanoribbons. The unit of energy is eV.

| Edge structure | $E_{ad}$ |
|---|---|
| *c*ACNR | 0.2263 |
| *c*ZZNR | 0.3555 |
| $H_v$-*c*ACNR | 1.0307 |
| $H_v$-*c*ZZNR | 0.3243 |

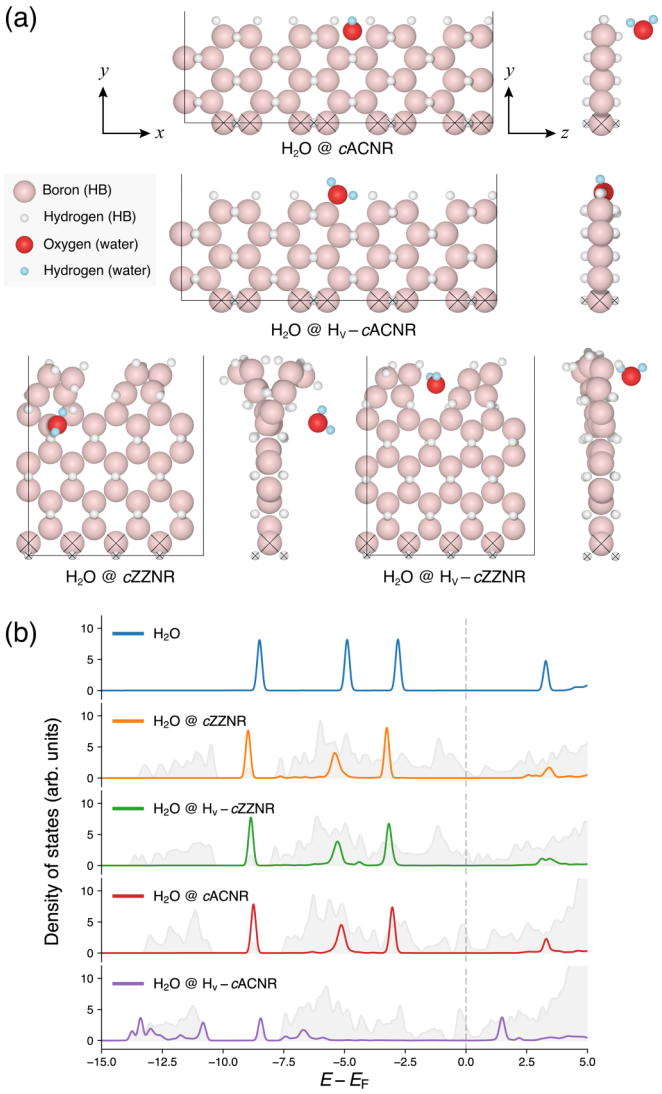


FIG. 4. (a) Optimized structures of water adsorption on armchair and zigzag HB nanoribbons, in both pristine and hydrogen-vacant cases. (b) Density of states projected onto the water molecular orbitals which were calculated as the sum of those onto the atomic orbitals of hydrogen and oxygen.

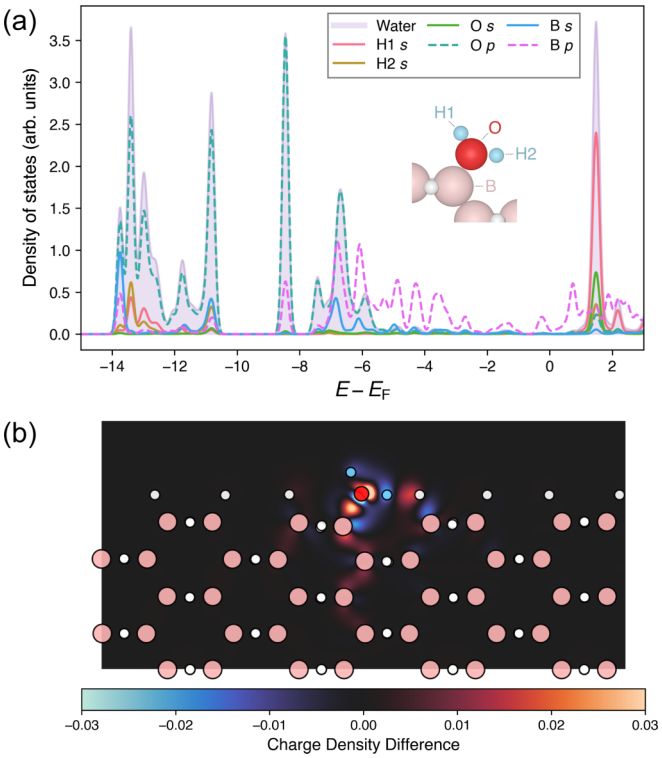


FIG. 5. Detailed electronic structure of water-adsorbed $H_v$-*c*ACNR. (a) Densities of states projected onto the atomic orbitals of B of HB at which water is adsorbed, H (H1,H2) and O of the water molecule. An inset showing the corresponding label on the structure was included. (b) Charge density difference.

The adsorption structures in Fig. 4(a) reveal consistent trends. For *c*ACNR, *c*ZZNR, and $H_v$-*c*ZZNR, the water molecule is positioned at a distance from the nanoribbon, with the molecule oriented such that the hydrogen atom serves as the primary point of interaction. In contrast to the aforementioned systems, the $H_v$-*c*ACNR shows that the oxygen atom of water is directly bonded to the edge B atom. This particular edge B atom is the collapsed one with a positive charge state as previously discussed. It is worth noting that the adsorption of water on $H_v$-*c*ACNR resulted in the recovery of the hexagonal boron that was previously collapsed by the hydrogen vacancy.

The projected density of states (pDOS) of water is illustrated in Fig. 4(b). The pDOS of water positioned furthest from the nanoribbon is included as a reference to an isolated water molecule. Here, it is important to compare the peaks for water which represents its molecular orbitals. Deviations in peak shapes from the isolated case signify potential hybridization between the water molecule and the HBNR. For the *c*ZZNR and *c*ACNR, the peak shape was preserved after adsorption, indicating that there is no significant bonding between water and both nanoribbons. The pDOS for the $H_v$-*c*ZZNR features small peaks around −4 eV, suggesting that partial hybridization has started to develop, albeit very minimally. Further structural deterioration may result in a more reactive edge, thereby stronger hybridization. On the other hand, the pDOS of water on $H_v$-*c*ACNR displays significant alterations, including the emergence of new peaks and a considerable decrease in the magnitude of the distinct peaks for the molecular orbitals of water, demonstrating hybridization between water and $H_v$-*c*ACNR.

Further investigations were conducted to delve deeper into the interaction between water and $H_v$-*c*ACNR. Figure 5(a) presents the pDOS for specific atomic orbitals (i.e., the H and O atoms in water and edge B atoms) in order to further elucidate the nature of interaction. The overlap between O *p* and B *p* orbitals is evident in several broad peaks spanning from −8.5 eV to −6 eV, indicative of the electronic states that facilitate the O-B chemical bond. Additional support for this concept is presented in Fig. S6 [56]. In addition, a cross sectional plot of the $\Delta\rho$ is provided in Fig. 5(b). Situated near the midpoint of O and edge B atoms, a charge gain region developed upon adsorption. This charge distribution profile is indicative of covalent bonding, as opposed to the dipole-dipole interactions previously observed in less reactive interactions on the HB sheet surface [5]. This interaction closely resembles the attachment of the OH to a boron atom in borane, initiating the hydrolysis process.

The various indicators provides strong evidence that $H_v$-*c*ACNR chemically bonds with the oxygen of water. In particular, the bonding mechanism can be attributed to the hybridization between the O *p* and B *p* orbitals. This chemical bonding of water to the B edge may be considered to be an onset of the partial hydrolysis resulting to the creation of boric acid and hydrogen gas appearing in the previous experimental work [5].

### C. Near edge water dissociation

Chemisorption of the water molecule at $H_v$-ACNR with significantly large adsorption energy reported in the previous section motivated us to further investigate possible water dissociation at the edge. We assumed that a dissociated H atom of water terminated the terminal B atom and explored possible adsorption sites and configurations of OH on the pristine ACNR.

In the search for the dissociated final state, the most stable configuration found features an OH adsorbed on a B atom near the edge, as presented in Fig. 6(b). This adsorption caused the localized buckling of B atoms and resulted in an energy 0.3 eV lower than the (intact) water edge-bonded structure reported earlier. In the experiments, the pH initially decreased immediately after mixing HB with distilled water but then remained nearly unchanged. B-O peaks appeared in the Fourier transform infrared spectra, indicating that the OH group does not dissolve in water but instead forms B-OH bonds during hydrolysis and remained intact even after drying [5,45]. This behavior aligns with the structure identified in our calculations.

To further investigate the possible water dissociation mechanism near the HB edge, we examined $H_v$-ACNR near the edge and adsorption of intact water on it. We then performed nudged elastic band (NEB) [60,61] calculations starting from a water molecule adsorption on a stable $H_v$-ACNR near the edge [Fig. 6(b)] and obtained the activation energy of 0.86 eV for water dissociation [Fig. 6(a)]. On the reverse side, the water reformation requires 1.53 eV, suggesting that it is easier

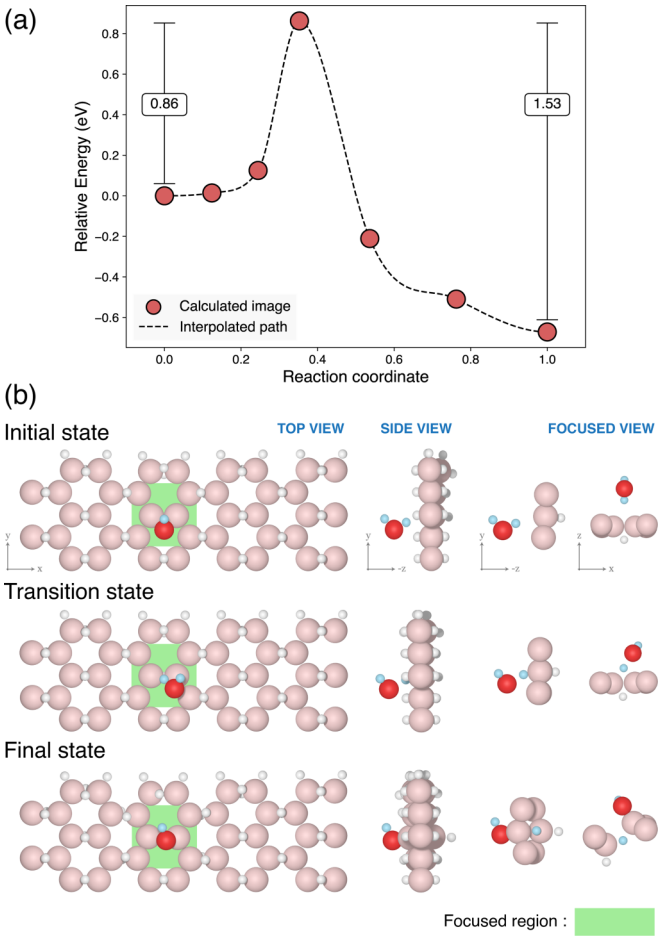


FIG. 6. Near edge water dissociation pathway on H-vacant HB sheets. The (a) energy profile illustrates the energy barriers associated with both forward and backward reactions. The energy baseline is referenced from the initial state, which corresponds to the water adsorbed on H-vacant HB sheets. The forward and backward reaction barrier are 0.86 eV and 1.53 eV, respectively. The (b) structures of the initial, transition and final states are shown from top and side perspectives. In addition, a focused view that incorporates $x$ and $y$ rotations are provided, displaying exclusively the atoms within the focused region (green) to enhance clarity.

to proceed with water dissociation than water reformation near the edge. Further analysis on the transition state revealed that the OH group is not isolated but is instead interacting significantly with the B atom underneath. This interaction is reflected in the pDOS by the delocalization of the O $2p$ states and their strong overlap with the B $2p$ states (see Fig. S11 [56]). Additionally, the comparison of the charge density difference profile with previous calculations [62] indicates that the OH group in the transition state behaves similarly to that of an $OH^-$ (see Fig. S12 [56]). However, since the OH group is not isolated, its impact on the system's energetics is expected to be insignificant when considering beyond standard DFT methods.

To compare the reactivity of surface and edge, a similar NEB calculation on water dissociation was performed on the HB sheet surface (Fig. S13 [56]). On the surface, the activation energy for the water dissociation is 0.96, which is higher than on the edge, meaning that water dissociation is easier to proceed near the edge as opposed to on the surface. This is due to the reduced prominence of the B-B bond network. While water dissociation is less favorable on the surface, hydrogen vacancies form more easily there, followed by the near edge and the terminal hydrogen site (Fig. S14 [56]). For a more accurate description of the reaction barrier, we performed single-point calculations at initial, transition, and final states using a range-separate hybrid van der Waals density functional [63]. These calculations showed an increase in the reaction barriers to 1.02 eV for edge reaction and 1.05 eV for the surface reaction (Fig. S15 [56]). Despite this increase, the overall trend remains consistent, with the edge reaction exhibiting a lower barrier than the surface reaction.

In the experiment, the reaction occurs in water, making it valuable to explore the effect of solvation on the reaction. The introduction of solvation effect, either explicit or implicit, is expected to lower the energy level of the transition state. The nucleophilic anion ($OH^-$) may be surrounded by layers of solvent molecules connected through hydrogen bonds, stabilizing the transition state, thereby lowering the reaction barrier [64]. Simulations that account for solvation effects may provide more quantitative insights into the reaction barriers and mechanism of the hydrolysis reaction, as well as the reactivity of the HB sheet, which remains a subject for future investigation.

Finally, we considered adsorption (binding) of an additional water molecule to OH of the dissociated water molecule (see Fig. S16 for the structure [56]). We obtained the progressive adsorption energy of 0.43 eV, which is larger than the binding energy of a water dimer (0.20 eV) and the interaction energy of a water dimer on a $H_v$ HB sheet [5] (0.18 eV), suggesting that the B-OH site provides a reactive site, which may attribute to the onset of hydrolysis.

## IV. SUMMARY AND CONCLUSIONS

This work examined two aspects of HB sheet nanoribbons: the relative stability of edge terminations and their reactivity with water. The ACNR was found to be more stable at all $H_2$ chemical potential range than the ZZNR. Additionally, the armchair edge preferred a 1:1 H/B termination ratio, while the zigzag edge leaned toward a 2:1 termination ratio. The optimization of the ZZNR − 2H structure resulted in a fringelike edge that was previously not observed. The removal of a hydrogen termination did not significantly affect edge structure of $c$ZZNR, however, $c$ACNR resulted in the collapse of the outer hexagon, with the collapsed boron showing a positive charge state.

Water was found to be physisorbed on various nanoribbons, except for the $H_v$-$c$ACNR, which exhibits a chemisorption behavior. The strong chemical interaction of water with the HB sheet may be one of the reasons for the partial hydrolysis reaction observed in the previous experiments.

Lastly, water dissociation was found to proceed on both edge and surface with significant activation energy, the latter requiring more. Thermodynamically, the water dissociated near the edge is more stable than the intact water adsorbed on the edge. This means that OH can terminate the near edge boron atoms, leading to an increase in reactivity that may have

an impact on applications that exploits the reactivity of HB sheets. In particular, catalytic behavior can change depending on the degree of passivation of the HB sheet.

The optimized structures of the HB sheet, along with sample input files referenced in this study, are accessible through the Materials Cloud Archive [65]. Additional data supporting the study's findings can be obtained from the corresponding authors upon reasonable request.

## ACKNOWLEDGMENTS

This work was supported by JST GteX (Grant No. JPMJGX23H1). Some of the calculations were performed using the facilities of the Supercomputer Center, Institute for Solid State Physics, The University of Tokyo, and the Cybermedia Center, Osaka University. K.I.M.R. would like to acknowledge the financial support provided by Ministry of Education, Culture, Sports, Science and Technology (MEXT), Japan.

[1] H. Nishino, T. Fujita, N. T. Cuong, S. Tominaka, M. Miyauchi, S. Iimura, A. Hirata, N. Umezawa, S. Okada, E. Nishibori, A. Fujino, T. Fujimori, S.-i. Ito, J. Nakamura, H. Hosono, and T. Kondo, J. Am. Chem. Soc. **139**, 13761 (2017).

[2] R. Kawamura, A. Yamaguchi, C. Shimada, R. Ishibiki, T. Fujita, T. Kondo, and M. Miyauchi, Chem. Lett. **49**, 1194 (2020).

[3] G. R. Eaton, Found. Chem. **25**, 285 (2023).

[4] T. Kondo, Chem. Lett. **52**, 611 (2023).

[5] K. I. M. Rojas, N. T. Cuong, H. Nishino, R. Ishibiki, S.-i. Ito, M. Miyauchi, Y. Fujimoto, S. Tominaka, S. Okada, H. Hosono, N. B. Arboleda, T. Kondo, Y. Morikawa, and I. Hamada, Commun. Mater. **2**, 81 (2021).

[6] I. Tateishi, N. T. Cuong, C. A. S. Moura, M. Cameau, R. Ishibiki, A. Fujino, S. Okada, A. Yamamoto, M. Araki, S. Ito, S. Yamamoto, M. Niibe, T. Tokushima, D. E. Weibel, T. Kondo, M. Ogata, and I. Matsuda, Phys. Rev. Mater. **3**, 024004 (2019).

[7] I. Tateishi, X. Zhang, and I. Matsuda, Molecules **27**, 1808 (2022).

[8] L. T. Ta, Y. Morikawa, and I. Hamada, J. Phys.: Condens. Matter **35**, 435002 (2023).

[9] Y. Jiao, F. Ma, J. Bell, A. Bilic, and A. Du, Angew. Chem., Int. Ed. **55**, 10292 (2016).

[10] B. Mortazavi, M. Makaremi, M. Shahrokhi, M. Raeisi, C. V. Singh, T. Rabczuk, and L. F. C. Pereira, Nanoscale **10**, 3759 (2018).

[11] J. He, D. Li, Y. Ying, C. Feng, J. He, C. Zhong, H. Zhou, P. Zhou, and G. Zhang, npj Comput. Mater. **5**, 47 (2019).

[12] R. Kawamura, N. T. Cuong, T. Fujita, R. Ishibiki, T. Hirabayashi, A. Yamaguchi, I. Matsuda, S. Okada, T. Kondo, and M. Miyauchi, Nat. Commun. **10**, 4880 (2019).

[13] M. Hikichi, J. Takeshita, N. Noguchi, S.-i. Ito, Y. Yasuda, L. T. Ta, K. I. M. Rojas, I. Matsuda, S. Tominaka, Y. Morikawa, I. Hamada, M. Miyauchi, and T. Kondo, Adv. Mater. Interfaces **10**, 2300414 (2023).

[14] S. Tominaka, R. Ishibiki, A. Fujino, K. Kawakami, K. Ohara, T. Masuda, I. Matsuda, H. Hosono, and T. Kondo, Chem **6**, 406 (2020).

[15] S. Kawamura, A. Yamaguchi, K. Miyazaki, S.-i. Ito, N. Watanabe, I. Hamada, T. Kondo, and M. Miyauchi, Small, **20** 2310239 (2024).

[16] T. A. Abtew, B.-c. Shih, P. Dev, V. H. Crespi, and P. Zhang, Phys. Rev. B **83**, 094108 (2011).

[17] T. A. Abtew and P. Zhang, Phys. Rev. B **84**, 094303 (2011).

[18] L. Chen, X. Chen, C. Duan, Y. Huang, Q. Zhang, and B. Xiao, Phys. Chem. Chem. Phys. **20**, 30304 (2018).

[19] P. Habibi, T. H. Saji, T. J. Vlugt, O. A. Moultos, and P. Dey, Appl. Surf. Sci. **603**, 154323 (2022).

[20] S. Gao, Y. Zhang, J. Bi, B. Wang, C. Li, J. Liu, C. Kong, S. Yang, and S. Yang, J. Mater. Chem. A **8**, 18856 (2020).

[21] S. Gao, H. Zhao, P. Gao, J. Bi, D. Liu, D. Zhu, B. Wang, and S. Yang, ACS Appl. Mater. Interfaces **14**, 34750 (2022).

[22] A. Saad, D. Liu, Y. Wu, Z. Song, Y. Li, T. Najam, K. Zong, P. Tsiakaras, and X. Cai, Appl. Catal. B: Environmental **298**, 120529 (2021).

[23] X. Zeng, Y. Jing, S. Gao, W. Zhang, Y. Zhang, H. Liu, C. Liang, C. Ji, Y. Rao, J. Wu, B. Wang, Y. Yao, and S. Yang, Nat. Commun. **14**, 7414 (2023).

[24] A. Fujino, S.-i. Ito, T. Goto, R. Ishibiki, J. N. Kondo, T. Fujitani, J. Nakamura, H. Hosono, and T. Kondo, ACS Omega **4**, 14100 (2019).

[25] A. Fujino, S.-i. Ito, T. Goto, R. Ishibiki, R. Osuga, J. N. Kondo, T. Fujitani, J. Nakamura, H. Hosono, and T. Kondo, Phys. Chem. Chem. Phys. **23**, 7724 (2021).

[26] T. Goto, S.-i. Ito, S. L. Shinde, R. Ishibiki, Y. Hikita, I. Matsuda, I. Hamada, H. Hosono, and T. Kondo, Commun. Chem. **5**, 118 (2022).

[27] S.-i. Ito, T. Hirabayashi, R. Ishibiki, R. Kawamura, T. Goto, T. Fujita, A. Yamaguchi, H. Hosono, M. Miyauchi, and T. Kondo, Chem. Lett. **49**, 789 (2020).

[28] N. Noguchi, S.-i. Ito, M. Hikichi, Y. Cho, K. Goto, A. Kubo, I. Matsuda, T. Fujita, M. Miyauchi, and T. Kondo, Molecules **27**, 8261 (2022).

[29] T. Hirabayashi, S. Yasuhara, S. Shoji, A. Yamaguchi, H. Abe, S. Ueda, H. Zhu, T. Kondo, and M. Miyauchi, Molecules **26**, 6212 (2021).

[30] N. T. Cuong, I. Tateishi, M. Cameau, M. Niibe, N. Umezawa, B. Slater, K. Yubuta, T. Kondo, M. Ogata, S. Okada, and I. Matsuda, Phys. Rev. B **101**, 195412 (2020).

[31] X. Zhang, Y. Tsujikawa, I. Tateishi, M. Niibe, T. Wada, M. Horio, M. Hikichi, Y. Ando, K. Yubuta, T. Kondo, and I. Matsuda, J. Phys. Chem. C **126**, 12802 (2022).

[32] T. Kondo, Science and Technology of Advanced Materials **18**, 780 (2017).

[33] J. M. Oliva-Enrich, T. Kondo, I. Alkorta, J. Elguero, and D. J. Klein, ChemPhysChem **21**, 2460 (2020).

[34] N. Ploysongsri, V. Vchirawongkwin, and V. Ruangpornvisuti, Vacuum **187**, 110140 (2021).

[35] N. Ploysongsri, V. Vchirawongkwin, and V. Ruangpornvisuti, Int. J. Hydrogen Energy **46**, 39273 (2021).

[36] B. Lei, Y.-Y. Zhang, and S.-X. Du, Chin. Phys. B **28**, 046803 (2019).

[37] M. Niibe, M. Cameau, N. T. Cuong, O. I. Sunday, X. Zhang, Y. Tsujikawa, S. Okada, K. Yubuta, T. Kondo, and I. Matsuda, Phys. Rev. Mater. **5**, 084007 (2021).

[38] V. Shukla, R. B. Araujo, N. K. Jena, and R. Ahuja, Phys. Chem. Chem. Phys. **20**, 22008 (2018).
[39] M. Makaremi, B. Mortazavi, and C. V. Singh, Mater. Today Energy **8**, 22 (2018).
[40] P. Xiang, X. Chen, B. Xiao, and Z. M. Wang, ACS Appl. Mater. Interfaces **11**, 8115 (2019).
[41] H. Li, B. Zhang, Y. Wu, J. Hou, D. Jiang, and Q. Duan, J. Phys. Chem. Solids **155**, 110108 (2021).
[42] R. L. Kumawat, M. K. Jena, and B. Pathak, J. Phys. Chem. C **124**, 27194 (2020).
[43] Y. An, Y. Hou, H. Wang, J. Li, R. Wu, T. Wang, H. Da, and J. Jiao, Phys. Rev. Appl. **11**, 064031 (2019).
[44] H. Nishino, T. Fujita, A. Yamamoto, T. Fujimori, A. Fujino, S.-i. Ito, J. Nakamura, H. Hosono, and T. Kondo, J. Phys. Chem. C **121**, 10587 (2017).
[45] S.-i. Ito, M. Hikichi, N. Noguchi, M. Yuan, Z. Kang, K. Fukuda, M. Miyauchi, I. Matsuda, and T. Kondo, Phys. Chem. Chem. Phys. **25**, 15531 (2023).
[46] P. Giannozzi, S. Baroni, N. Bonini, M. Calandra, R. Car, C. Cavazzoni, D. Ceresoli, G. L. Chiarotti, M. Cococcioni, I. Dabo, A. D. Corso, S. de Gironcoli, S. Fabris, G. Fratesi, R. Gebauer, U. Gerstmann, C. Gougoussis, A. Kokalj, M. Lazzeri, L. Martin-Samos *et al.*, J. Phys.: Condens. Matter **21**, 395502 (2009).
[47] P. Giannozzi, O. Andreussi, T. Brumme, O. Bunau, M. B. Nardelli, M. Calandra, R. Car, C. Cavazzoni, D. Ceresoli, M. Cococcioni, N. Colonna, I. Carnimeo, A. D. Corso, S. de Gironcoli, P. Delugas, R. A. DiStasio, A. Ferretti, A. Floris, G. Fratesi, G. Fugallo *et al.*, J. Phys.: Condens. Matter **29**, 465901 (2017).
[48] P. Giannozzi, O. Baseggio, P. Bonfà, D. Brunato, R. Car, I. Carnimeo, C. Cavazzoni, S. de Gironcoli, P. Delugas, F. Ferrari Ruffino, A. Ferretti, N. Marzari, I. Timrov, A. Urru, and S. Baroni, J. Chem. Phys. **152**, 154105 (2020).
[49] R. Sabatini, E. Küçükbenli, B. Kolb, T. Thonhauser, and S. de Gironcoli, J. Phys.: Condens. Matter **24**, 424209 (2012).
[50] T. Thonhauser, V. R. Cooper, S. Li, A. Puzder, P. Hyldgaard, and D. C. Langreth, Phys. Rev. B **76**, 125112 (2007).
[51] K. F. Garrity, J. W. Bennett, K. M. Rabe, and D. Vanderbilt, Comput. Mater. Sci. **81**, 446 (2014).
[52] D. Vanderbilt, Phys. Rev. B **41**, 7892 (1990).
[53] I. Hamada, Phys. Rev. B **89**, 121103(R) (2014).
[54] M. Callsen and I. Hamada, Phys. Rev. B **91**, 195103 (2015).
[55] Y. Hamamoto, I. Hamada, K. Inagaki, and Y. Morikawa, Phys. Rev. B **93**, 245440 (2016).
[56] See Supplemental Material at http://link.aps.org/supplemental/10.1103/PhysRevMaterials.8.114004 for additional details and further discussion on formation energies, structural models of H-terminated HB nanoribbons, charge analysis, O-B (OH-B) bonding, water dissociation pathways, and additional water adsorption, which includes Refs. [66–68].
[57] M. W. Chase, *NIST-JANAF Thermochemical Tables*, 4th ed. (American Institute of Physics, 1998).
[58] S. A. Wella, Y. Hamamoto, Suprijadi, Y. Morikawa, and I. Hamada, Nanoscale Adv. **1**, 1165 (2019).
[59] L. Zhu, B. Zhao, T. Zhang, G. Chen, and S. A. Yang, J. Phys. Chem. C **123**, 14858 (2019).
[60] H. Jónsson, G. Mills, and K. W. Jacobsen, Nudged elastic band method for finding minimum energy paths of transitions, in *Classical and Quantum Dynamics in Condensed Phase Simulations* (World Scientific, 1998), pp. 385–404.
[61] G. Henkelman, B. P. Uberuaga, and H. Jónsson, J. Chem. Phys. **113**, 9901 (2000).
[62] I. Hamada, T. Kumagai, A. Shiotari, H. Okuyama, S. Hatta, and T. Aruga, Phys. Rev. B **86**, 075432 (2012).
[63] V. Shukla, Y. Jiao, J.-H. Lee, E. Schröder, J. B. Neaton, and P. Hyldgaard, Phys. Rev. X **12**, 041003 (2022).
[64] S. K. Desai and M. Neurock, Phys. Rev. B **68**, 075420 (2003).
[65] K. I. Rojas, Y. Morikawa, and I. Hamada, Materials Cloud Archive **2024** (2024).
[66] Q. Zhang and A. Asthagiri, Catal. Today **323**, 35 (2019).
[67] W. Yang, D. Wei, X. Jin, C. Xu, Z. Geng, Q. Guo, Z. Ma, D. Dai, H. Fan, and X. Yang, J. Phys. Chem. Lett. **7**, 603 (2016).
[68] D. S. Potts, D. T. Bregante, J. S. Adams, C. Torres, and D. W. Flaherty, Chem. Soc. Rev. **50**, 12308 (2021).